Controllable synthesis and phase-dependent catalytic performance of dual-phase nickel selenides on Ni foam for overall water splitting

Lei Tan [a], Jiangtao Yu [a], Haiyan Wang [a], Hongtao Gao [a], Xien Liu [a], Lei Wang [a], Xilin She [b], Tianrong Zhan [a],*

[a] Key Laboratory of Optic-electric Sensing and Analytical Chemistry for Life Science (Ministry of Education), State Key Laboratory Base of Eco-chemical Engineering, Qingdao University of Science and Technology, Qingdao 266042, PR China
[b] School of Environmental Science and Engineering, Collaborative Innovation Center for Marine Biomass Fiber, Materials and Textiles of Shandong Province, Qingdao University, Qingdao 266071, PR China

ARTICLE INFO

ABSTRACT

$NiSe_2/Ni_3Se_4$ dual-phase electrocatalysts are synthesized by calcining the $Ni(OH)_2$ nanosheets on Ni foam and Se powder under an N_2 atmosphere. The Ni's charge-state, phase compositions, and electrocatalytic performances are dependent on the initial mass ratios of Ni to Se. The experimental results demonstrate that the electrocatalyst with a higher Ni charge-state and more Ni_3Se_4 phase facilitates oxygen evolution reaction (OER), whereas the one with a lower Ni charge-state and more $NiSe_2$ phase boosts hydrogen evolution reaction (HER). Density functional theory calculations reveal that the interfacial electrons transfer from Ni_3Se_4 to $NiSe_2$, which improves conductivity and optimizes adsorption/desorption energies. $NiSe_2/Ni_3Se_4/NF-4$ containing more $NiSe_2$ phase displays the best HER activity while $NiSe_2/Ni_3Se_4/NF-1$ containing more Ni_3Se_4 phase shows the best HER activity. The electrolyzer, employing $NiSe_2/Ni_3Se_4/NF-4$ and $NiSe_2/Ni_3Se_4/NF-1$ as the cathode and anode, respectively, performs the full potential and demonstrates a low voltage of 1.56 V achieving 10 mA cm^{-2} with good durability.

1. Introduction

The solar energy-driven electrochemical splitting of water into oxygen and hydrogen is a sustainable energy conversion and storage technology that can cater to energy demand and alleviate carbon emissions stemming from the excess consumption of fossil fuel [1,2]. The water-splitting involves two central processes: hydrogen evolution reaction (HER) at the cathode and oxygen evolution reaction (OER) at the anode. Unfortunately, OER and HER are plagued by their sluggish kinetics, which needs to be boosted by state-of-the-art electrocatalysts (such as Ru- or Ir-based for OER, whereas Pt-based for HER) [3,4]. However, the small earth abundance, high price, and poor long-term stability dramatically circumscribe their large-scale applications. Numerous efforts have been made in the development of nonprecious metal electrocatalysts with high activity and durability for electrochemical water-splitting. The reported electrocatalysts include transition metal sulfides [5], carbides [6], selenides [7], and phosphides [8] for HER electrocatalysis, and transition-metal (hydro)oxides for OER electrocatalysis [9–11]. Note that HER electrocatalysts perform well in

acidic electrolytes, while OER ones work better under alkali conditions. The pH mismatch of the combined OER and HER electrocatalysts could inevitably bring out inferior water-splitting performance. Although bifunctional electrocatalysts for both HER and OER have been developed to simplify the water-splitting system and lower the cost, they commonly display excellent HER activity with relatively poor OER catalytic activity and vice versa [2–5,10,12].

Nickel selenides have emerged as a new type of transition metal chalcogenide and received a high reputation in the field of electrocatalysis because of their high electrical conductivity, low band gaps, high chemical stability, and low cost [12]. Impressively, nickel selenides possess a lower H-desorption bond energy (276 kJ mol^{-1}) than metal sulfides (363 kJ mol mol^{-1}), and metal phosphides (322 kJ mol mol^{-1}), which allows them as good candidates for HER electrocatalysts [13,14]. For instance, reports have shown that NiSe and $NiSe_2$ nanostructures exhibit excellent HER catalytic activities [15,16]. On the other side, nickel selenides also reveal good OER catalytic capability due to the existence of a localized negative charge on Se sites [15]. The smaller electronegativity of Se element (2.55) than that of O element (3.44)

* Corresponding author.
  E-mail address: trzhan@qust.edu.cn (T. Zhan).

results in the superior OER activity of Ni-selenide (Ni_3Se_2) to that of Ni-oxide/hydroxides [17]. For example, Ni_3Se_2 displays better OER catalytic activity than the other Ni-based materials of NiO, NiSe, and Ni due to the synergetic advantages of metallic character and facile surface reorganization [18]. A nanocoral-like $NiSe_2$/g-C_3N_4 composite demonstrates the high OER activity for water oxidation in a 1.0 M KOH solution [19]. Some nickel selenide phases, such as $Ni_{0.95}Se$ [14], $NiSe_2$ [20], Ni_3Se_2 [21], and Ni_3Se_4 [22], manifest bifunctional catalytic activities, however, most of these single-phase catalysts only exhibit outstanding HER or OER catalytic performance. Anyway, this survey has established that the HER or/and OER performances are strongly dependent on the ratio of Se to Ni [22,23]. Tuning the stoichiometry of Se to Ni can fabricate the multi-phase nickel selenides with excellent HER or/and OER catalytic activity. Several dual-phase nickel selenides have been recently reported as appealing bifunctional catalysts for alkaline water splitting [24–26]. Nevertheless, the aforementioned strategies remain several issues. For example, real active sites for HER or OER are unclear due to the complicated phase compositions. Whether the target bifunctional catalyst presents the best both HER and OER catalytic activity needs to be further investigated since the activity is highly dependent on the phase composition. Particularly, despite prominent HER or/and OER activities of $NiSe_2$ and Ni_3Se_4, to date, there is no reported study on the preparation and the phase-dependent catalytic mechanism of the dual-phase $NiSe_2$/Ni_3Se_4 catalysts.

Herein, we report the fabrication of novel 3D free-standing dual-phase nickel selenide electrodes consisting of $NiSe_2$ and Ni_3Se_4 with rich-phase boundaries ($NiSe_2$/Ni_3Se_4/NF). The dual-phase catalyst electrodes were prepared by selenizing the $Ni(OH)_2$ species in situ grown on Ni foam with Se powder in a tube furnace. The phase composition, the charge state of Ni species (relative mole ratio of Ni^{3+}/Ni^{2+}), and electrocatalytic performance of the nickel selenide catalysts are manipulated by adjusting the initial mass of Se powder. The mechanism study demonstrates that a high Ni charge state and more Ni_3Se_4 phase facilitate OER performance, while a low Ni charge state and more $NiSe_2$ phase favor HER activity. Moreover, the experimental and density functional theory (DFT) results verify that the dual-phase synergism can effectively boost their intrinsic HER and OER activities in alkaline medium, whereas the $NiSe_2$ and Ni_3Se_4 phases are mainly responsible for HER and OER activities, respectively. Consequently, $NiSe_2$/Ni_3Se_4/NF-4 containing more $NiSe_2$ phase displays the best HER activity while $NiSe_2$/Ni_3Se_4/NF-1 containing more Ni_3Se_4 phase shows the best HER activity. The eminent catalytic performance originates from more available active sites and fast mass transfer provided by the as-prepared 3D $NiSe_2$/Ni_3Se_4 heterostructures. When $NiSe_2$/Ni_3Se_4/NF-4 and $NiSe_2$/Ni_3Se_4/NF-1 are respectively employed as the cathode and anode for overall water-splitting, the electrolyzer will perform its full potential and delivers a low voltage of only 1.56 V at a current density of 10 mA cm^{-2}.

2. Experimental section

2.1. Chemicals

The potassium phosphate dibasic trihydrate ($K_2HPO_4 \cdot 3H_2O$, 99.0%), potassium hydroxide (KOH, ≥85%), and Selenium powder (Se, 99.9%) were purchased from Aladdin regent Co. Ltd (Shanghai, China). Ni foam (NF, porosity: 99.8%, PPI: 110) was purchased from Shengernuo Technology Co. Ltd (Suzhou, China). Ultrapure water with resistivity >18 MΩ cm^{-1} was used. All chemicals were used as received without any further purification.

2.2. Synthesis of $Ni(OH)_2$/NF

Ni foam was cut into 2.5 × 4 cm^2 plates, which were respectively ultrasonically treated with 3 M HCl aqueous solution, deionized water, and ethanol for 30, 5, 10 min to remove the surface oxides and organic molecules, and then dried at 50 °C for 6 h. The $Ni(OH)_2$/NF was obtained via a two-step hydrothermal method. First, one piece of Ni foam (2.5 × 4 cm^2) was immersed into 35 ml of a K_2HPO_4 solution (1 mM) in a 50 ml Teflon autoclave and then hydrothermally treated for 12 h at 180 °C. After naturally cooling to room temperature, the achieved precursors were washed several times with deionized water and dried at 50 °C for 6 h. Second, the green precursors were transformed into a 50 ml Teflon autoclave containing 30 ml 0.1 M KOH aqueous solution and then hydrothermally reacted at 120 °C for 5 h. The light gray $Ni(OH)_2$/NF nanoarrays were obtained after washing with deionized water followed by natural drying at 50 °C overnight.

2.3. Synthesis of $NiSe_2$/Ni_3Se_4/NF catalysts

$NiSe_2$/Ni_3Se_4/NF catalysts were prepared via a low-temperature calcination method using a horizontal tube furnace. The $Ni(OH)_2$/NF and different qualities of Se powder (0.1, 0.2, 0.3, 0.4, and 0.5 g) were placed at the downstream and upstream sides of the tube furnace, respectively. Under an N_2 atmosphere, the furnace was heated to 300 °C with a heating ramp of 3 °C min^{-1} and kept this temperature until the Se powder was completely volatilized. During the whole process, the flow of N_2 was maintained at a rate of 80 sccm. After naturally cooling to room temperature, the black samples were afforded and respectively denoted as $NiSe_2$/Ni_3Se_4/NF-1, $NiSe_2$/Ni_3Se_4/NF-2, $NiSe_2$/Ni_3Se_4/NF-3, $NiSe_2$/Ni_3Se_4/NF-4, and $NiSe_2$/Ni_3Se_4/NF-5, which were used for subsequent structural characterizations and electrochemical tests.

For comparison, the pure $NiSe_2$ phase was prepared by a thermal selenization of the cleaned NF at 550 °C in the N_2 atmosphere for 1 h with the Se powder. The pure Ni_3Se_4 phase was prepared by a thermal selenization of the prepared $Ni(OH)_2$/NF at 550 °C in the N_2 atmosphere for 1 h with the Se powder.

2.4. Characterizations

The phase compositions were characterized by a Japan X-ray diffractometer (XRD, Rigaku, D/MAX/2500 PC) equipped with Cu Kα radiation (λ = 1.54056 Å). The morphologies were analyzed by field emission scanning electron microscopy (FE-SEM, SU 8000) and transmission electron microscopy (TEM, JEOL JEM-2000EX). The X-ray photoelectron spectra (XPS) were performed using an XPS apparatus (AXIS SUPRA) and the obtained binding energies were corrected for specimen charging by referencing C 1s to 284.6 eV. The chemical component analysis was determined by Inductively Coupled Plasma-Atomic Emission Spectrometry (ICP-AES) using Agilent ICPOES 7800 spectrometer.

2.5. Electrochemical measurements

All electrochemical measurements were carried out on a CHI 660D electrochemical workstation at room temperature. The HER and OER performances were measured in a 1.0 M KOH solution by a three-electrode cell with a graphite rod counter electrode, an Hg/HgO reference electrode, and the obtained catalysts on Ni foam as the working electrode (1 ×1 cm^2). The catalyst loading is estimated to be 7.4 ± 0.3 mg/cm^2. The linear sweep voltammetry (LSV) curves were performed at a scan rate of 2 mV s^{-1} with 80% iR compensation. The corresponding Tafel plots were obtained by fitting the polarization curves between the overpotential (η) and log current density (log j) via the equation: $\eta = b\log(j) + a$, where the b is the Tafel slope. The double-layer capacitance (C_{dl}) values were obtained from the cyclic voltammetry (CV) curves in the double-layer region (without Faradaic processes) in the potential ranges from 0.024 to 0.174 V for HER and from 0.924 to 1.074 V for OER at different scan rates. The corresponding linear slope is twice the C_{dl}. The electrochemical surface area (ECSA) can be calculated according to the equation of ECSA = C_{dl}/C_s. C_s is the specific capacitance ranging between 0.022 and 0.130 mF cm^{-2} in alkaline solution. Here we use the value of C_s to be 0.040 mF cm^{-2} based on the previous report [17].

Electrochemical impedance spectroscopy (EIS) measurements were carried out in a frequency range of from 100 kHz to 0.1 Hz with an amplitude of 5 mV. The long-term durability test was performed using chronoamperometry at a constant current density. All measured potentials were displayed versus the reversible hydrogen electrode (RHE) according to the equation of $E_{RHE} = E_{Hg/HgO} + 0.059$ pH $+ 0.098$ V. Overall water-splitting measurements were carried out in a two-electrode system consisting of the sample $NiSe_2/Ni_3Se_4/NF$ as cathode and anode.

2.6. Theoretical calculations

In this work, the electronic structure and electrochemical properties of 2D Ni_2Se/Ni_3Se_4 composites are investigated via first-principles simulations. Computational simulations of density functional theory (DFT) were carried out by using the Vienna ab-initio simulation package (VASP) with the projector augmented wave (PAW) method to describe the ionic cores. The Perdew-Burke-Ernzerhof (PBE) functional within the generalized gradient approximation (GGA) was performed to describe electronic exchange-correlation energy. The plane wave energy cutoff was set to 400 eV. The Brillouin zone was sampled at Gamma point with the $1 \times 3 \times 1$ k-points grid for the surface of the experimental sample. Since the reaction occurs on the surface, in all structural optimization calculations, atoms of the bottom layer were fixed, while the positions of other atoms were allowed to relax. A vacuum region of 20 Å was applied to the vertical direction to avert interactions between the neighboring layers. The energy and force criterion for convergence of the electron density was set to 10^{-4} eV and 0.05 eV/Å, respectively.

3. Results and discussion

3.1. Structural characterization

The synthesis of the $NiSe_2/Ni_3Se_4/NF$ electrodes is schematically illustrated in Fig. 1. The optical photos of prepared samples were presented in Fig. S1. To ensure more active sites available and large surface area, the free-standing $Ni(OH)_2$ nanosheets on the NF were first synthesized by the hydrothermal treatment with K_2HPO_4 and KOH solutions in turn. The SEM images in Fig. S2 exhibit the uniform distribution of $Ni(OH)_2$ nanosheets with a lateral size of ca. 2–4 μm. The cross-section SEM image in the inset of Fig. S2b reveals that the length of $Ni(OH)_2$ nanosheets is about 10–14 μm. Then the light green $Ni(OH)_2$ precursor was annealed at 300 ℃ under an N_2 flow by placing different amounts of Se powder (0.1, 0.2, 0.3, 0.4, and 0.5 g) at the upper location of the tube furnace. Correspondingly, the five black dual-phase catalyst electrodes were obtained ($NiSe_2/Ni_3Se_4/NF$-1, $NiSe_2/Ni_3Se_4/NF$-2, $NiSe_2/Ni_3Se_4/NF$-3, $NiSe_2/Ni_3Se_4/NF$-4, and $NiSe_2/Ni_3Se_4/NF$-5). The SEM images (Fig. S3) and XRD patterns (Fig. 2a) of these five samples were analyzed to elucidate their phase changes with increasing the Se powder amount. SEM images indicate that the lamellar Ni_3Se_4 [27] phase decreases first then increases whereas the polyhedral $NiSe_2$ [28] phase exhibits a reverse trend. The $NiSe_2/Ni_3Se_4/NF$-4 sample harvests the most polyhedron phases containing a few nanosheets with distinct boundaries (Fig. S3d' and d1). The XRD patterns confirm that all five products are composed of $NiSe_2$ (JCPDS no. 88–1711) and Ni_3Se_4 (JCPDS no.

89–2020) phases without other impurities. Based on the XRD data, the semi-quantitative results of their composition are obtained by using the Highscore software [29] as shown in Fig. S4. The percentage of Ni_3Se_4 in five samples gives a descending fashion whereas that of $NiSe_2$ displays an ascending mode against the increasing Se powder from 0.1 to 0.5 g, demonstrating a transition of Ni-rich to Se-rich selenides.

X-ray photoelectron spectroscopy (XPS) measurements were then carried out to further analyze the surface compositions and the chemical states. Fig. S5a describes the survey XPS spectrum of five $NiSe_2/Ni_3Se_4/NF$ electrodes, which testify to the presence of Ni and Se in all samples. The different bonding states of Ni 2p for all $NiSe_2/Ni_3Se_4/NF$ catalysts were verified by their Ni 2p XPS spectra as illustrated in Fig. 2b. All samples show two core-level peaks of Ni located at about 855 and 873 eV, which are assigned to Ni $2p_{3/2}$ and Ni $2p_{1/2}$ accompanied by their satellite peaks at relatively higher binding energies, respectively [4]. After deconvolution, two peaks at ~853 and ~855 eV for the Ni $2p_{2/3}$ are responsible for Ni^{2+} and Ni^{3+}, respectively. Two peaks at ~870 and ~873 eV for the Ni $2p_{1/3}$ are attributed to Ni^{2+} and Ni^{3+}, respectively [30]. The relative mole ratios of Ni^{3+}/Ni^{2+} of the catalysts gradually decrease from 1.442 to 1.105 when increasing the Se powder from 0.1 g to 0.5 g. It should be noted that the mole ratios of Ni^{3+} to Ni^{2+} for $NiSe_2/Ni_3Se_4/NF$-1 and $NiSe_2/Ni_3Se_4/NF$-4 are more close to those for pure Ni_3Se_4 (3.06) and $NiSe_2$ (1.00), respectively (Fig. S5d). The comprehensive results indicate that the content of Ni^{3+} becomes more whereas that of Ni^{2+} does less upon the increase of Se powder. The Se 3d XPS spectra of all catalysts are shown in Fig. S5b, in which two peaks at ~ 54 and ~ 55 eV are attributable to Se $3d_{5/2}$ and $3d_{3/2}$, respectively. The broad peak at about 58.5 eV manifests the presence of SeO_x in all samples due to the surface oxidation [31].

Among this series of dual-phase catalysts, $NiSe_2/Ni_3Se_4/NF$-4 exhibits the best HER activity, and $NiSe_2/Ni_3Se_4/NF$-1 shows the optimal OER performance. Therefore, SEM and transmission electron microscopy (TEM) images of these two samples were further analyzed to study their microstructure and morphology. SEM images reveal that both free-standing electrodes show a 3D network consisting of nanosheets and polyhedral units (Fig. S3a, a', d, and d'). Intriguingly, $NiSe_2/Ni_3Se_4/NF$-1 owns the more lamellar phase and fewer polyhedral crystals and $NiSe_2/Ni_3Se_4/NF$-4 shows the opposite situation. TEM images (Fig. 3a and e) exhibit that there exist nanoparticles and nanosheets in both catalysts. HRTEM images of $NiSe_2/Ni_3Se_4/NF$-1 demonstrate distinct lattice fringes with interplanar spacings of 0.263 and 0.201 nm that refer to the $NiSe_2$ (210) and Ni_3Se_4 (−514) plane, respectively (Fig. 3b–d). Similarly, the above-mentioned lattice fringes are also found in $NiSe_2/Ni_3Se_4/NF$-4 with interplanar spacings of 0.267 and 0.204 nm corresponding to the $NiSe_2$ (210) and Ni_3Se_4 (−514) plane, respectively (Fig. 3f–h). Visible phase boundaries between $NiSe_2$ and Ni_3Se_4 crystalline identify a lot of lattice mismatch, which indicates the successful fabrication of the heterointerface in the dual-phase electrocatalyst [32]. This unique heterostructure could effectively create more defects, make more active sites available, and shorten the mass transport pathway in electrocatalysis when they are employed as electrode materials [33–35].

3.2. Electrocatalytic activity

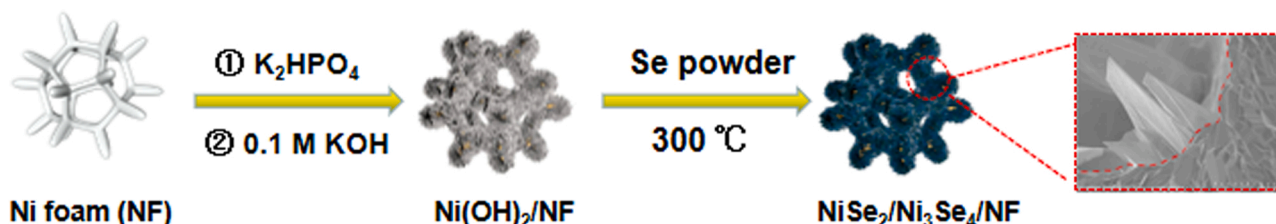The HER activities of the $NiSe_2/Ni_3Se_4/NF$-4 and $NiSe_2/Ni_3Se_4/NF$-1

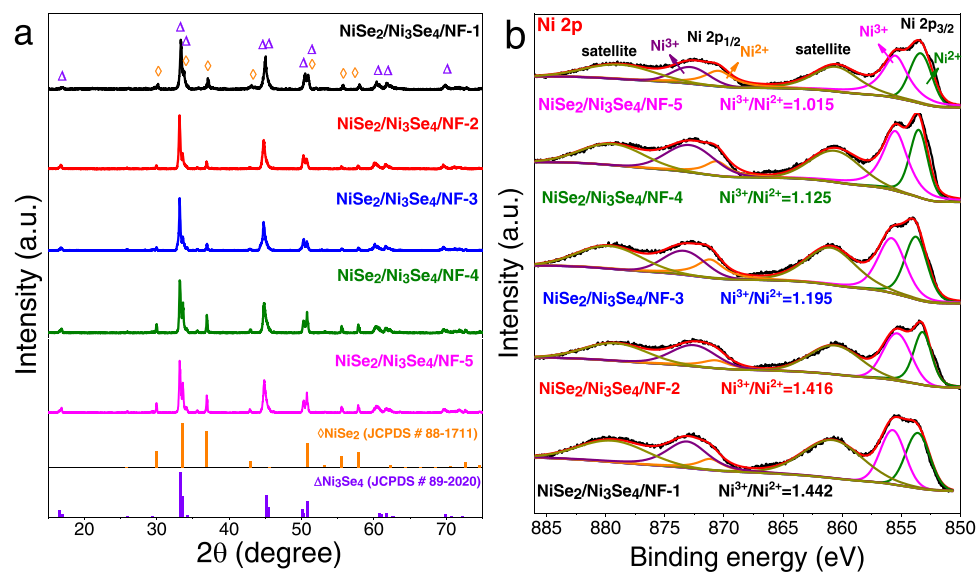**Fig. 1.** Schematic illustration for the preparation of the $NiSe_2/Ni_3Se_4/NF$ samples.

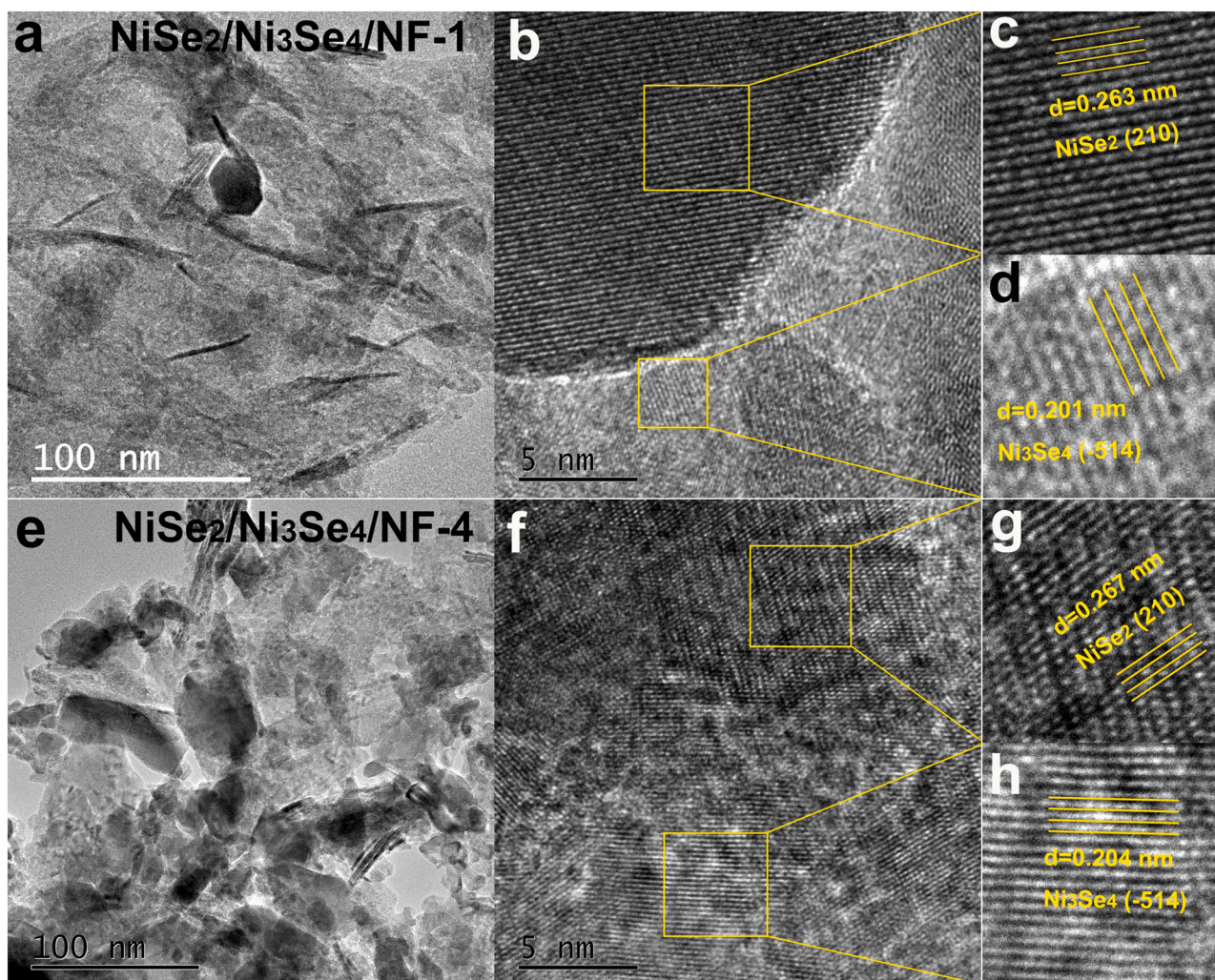**Fig. 2.** The XRD patterns (a) and Ni 2p XPS (b) spectra of the series of NiSe$_2$/Ni$_3$Se$_4$/NF catalysts.

Fig. 3. TEM and HRTEM images of NiSe$_2$/Ni$_3$Se$_4$/NF-1 (a–d) and NiSe$_2$/Ni$_3$Se$_4$/NF-4 (e–h).
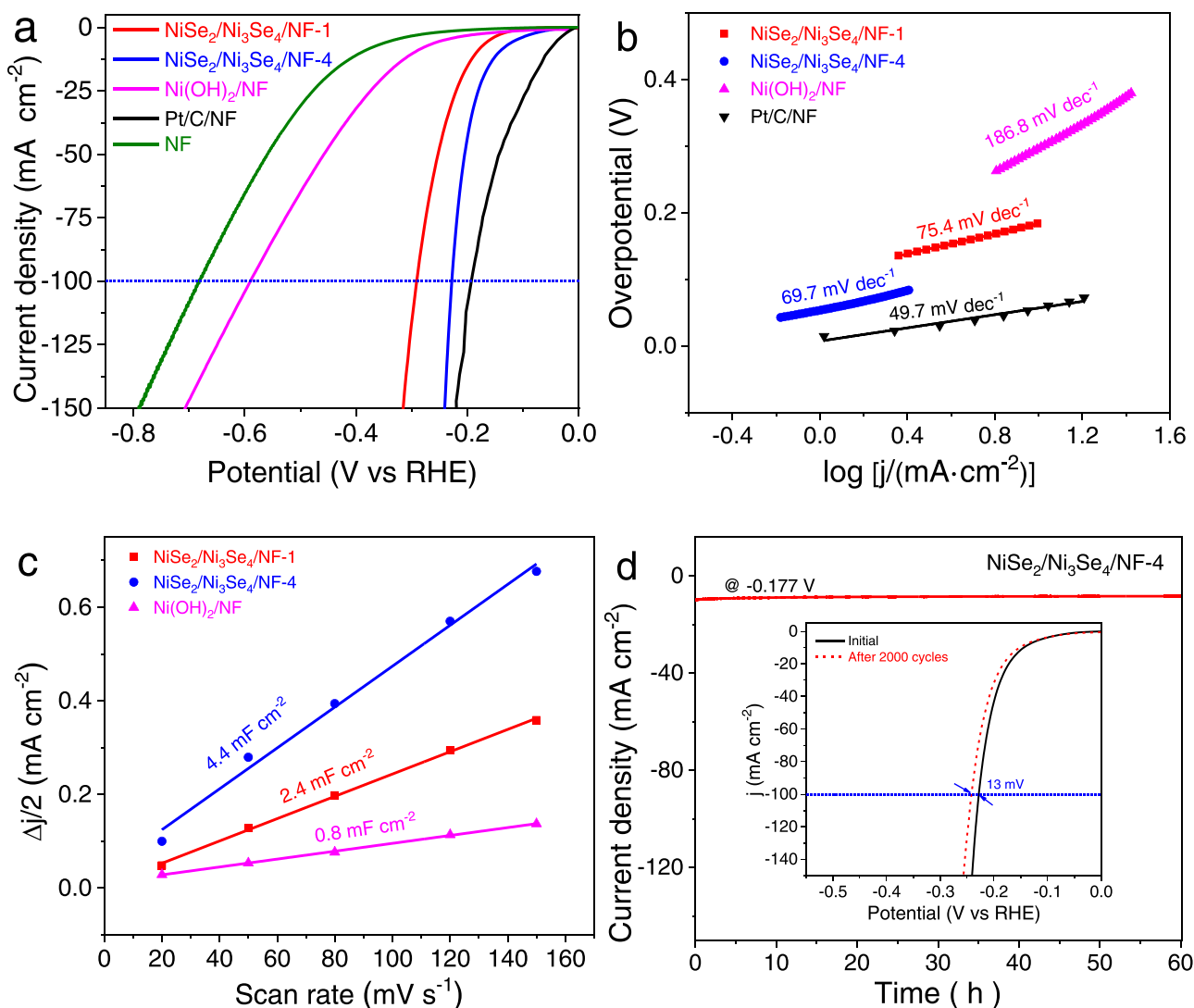
Fig. 4. (a) Polarization curves of NiSe$_2$/Ni$_3$Se$_4$/NF-1, NiSe$_2$/Ni$_3$Se$_4$/NF-4, Ni(OH)$_2$/NF, bare NF, and 20 wt% Pt/C/NF performed at a scan rate of 2 mV s^{-1} for HER in 1.0 M KOH. (b) Their corresponding Tafel plots. (c) The capacitive current difference at 0.099 V (vs RHE) plotted upon the scan rate for the assessment of the double-layer capacitance. (d) The chronoamperometric curve for NiSe$_2$/Ni$_3$Se$_4$/NF-4 at a constant potential of -0.177 V (vs RHE) for 60 h without iR correction. Inset: Polarization curves of the initial and after 2000 CV cycles for NiSe$_2$/Ni$_3$Se$_4$/NF-4 with iR correction.

electrodes were firstly evaluated in 1.0 M KOH electrolytes via a three-electrode system at room temperature. Bare NF and 20 wt% Pt/C loaded on NF were also selected for comparison. Fig. 4a shows polarization curves performed at a scan rate of 2 mV s^{-1} on the reversible hydrogen electrode (RHE) scale with iR correction. It can be seen that the performance of the NiSe$_2$/Ni$_3$Se$_4$/NF-4 is only inferior to that of the Pt/C/NF but much better than those of NiSe$_2$/Ni$_3$Se$_4$/NF-1, Ni(OH)$_2$/NF, and bare NF. The NiSe$_2$/Ni$_3$Se$_4$/NF-4 electrode achieving a current density of 10 mA cm^{-2} only requires an overpotential of 145 mV, which is much lower than those of NiSe$_2$/Ni$_3$Se$_4$/NF-1 (185 mV), Ni(OH)$_2$/NF (299 mV), and bare Ni foam (393 mV). Besides, this overpotential compares favorably to those of other reported HER catalysts such as NiSe$_2$@NG (248 mV) [36], MN-Ni$_3$Se$_4$/MoSe$_2$ (160 mV) [21], and NiFe-LDH@Cu$_2$Se/NF (195 mV) [4] in 1.0 M KOH (see the comparison in Table S1). Notably, to reach a current density of 100 mA cm^{-2} NiSe$_2$/Ni$_3$Se$_4$/NF-4 only needs an overpotential of 228 mV, which is moderately bigger than that for Pt/C/NF (194 mV) but distinctly lower than those for NiSe$_2$/Ni$_3$Se$_4$/NF-1 (291 mV) and the reported CoSe/Co$_9$Se$_8$ catalyst (268 mV) [37]. The results further indicate the superior performance of NiSe$_2$/Ni$_3$Se$_4$/NF-4 toward the HER. The Tafel plots of

NiSe$_2$/Ni$_3$Se$_4$/NF-4, NiSe$_2$/Ni$_3$Se$_4$/NF-1, Pt/C/NF, and Ni(OH)$_2$/NF for HER processes are presented in Fig. 4b. Pt/C on the NF affords a Tafel slope of about 49.7 mV dec^{-1}, which is close to the reported value [38]. The Tafel slope of NiSe$_2$/Ni$_3$Se$_4$/NF-4 is 69.7 mV dec^{-1}, which is larger than that of the Pt/C/NF but visibly smaller than those of NiSe$_2$/Ni$_3$Se$_4$/NF-1 (75.4 mV dec^{-1}) and Ni(OH)$_2$/NF (186.8 mV dec^{-1}), revealing a favorable HER kinetics for NiSe$_2$/Ni$_3$Se$_4$/NF-4. The slopes of NiSe$_2$/Ni$_3$Se$_4$/NF-4 and NiSe$_2$/Ni$_3$Se$_4$/NF-1 are in the range of 40–120 mV dec^{-1}, manifesting that a Volmer–Heyrovsky mechanism for their HER processes [39].

The ECSA values of NiSe$_2$/Ni$_3$Se$_4$/NF-4, NiSe$_2$/Ni$_3$Se$_4$/NF-1, and Ni(OH)$_2$/NF are further estimated by measuring their C_{dl} in the potential region from 0.024 to 0.174 V (vs RHE) (Fig. S6). The linear curves in Fig. 4c exhibit that the C_{dl} of NiSe$_2$/Ni$_3$Se$_4$/NF-4 (4.4 mF cm^{-2}) is much larger than those of NiSe$_2$/Ni$_3$Se$_4$/NF-1 (2.4 mF cm^{-2}), and Ni(OH)$_2$/NF (0.8 mF cm^{-2}), suggesting a larger ECSA with more exposed active sites and thus exhibiting a higher HER catalytic activity. To assess the intrinsic HER activity, we also calculated the specific activities of NiSe$_2$/Ni$_3$Se$_4$/NF-4, NiSe$_2$/Ni$_3$Se$_4$/NF-1, and Ni(OH)$_2$/NF concerning their estimated ECSA. As shown in Fig. S7a, NiSe$_2$/Ni$_3$Se$_4$/NF-4 was found to

outperform NiSe$_2$/Ni$_3$Se$_4$/NF-1 and Ni(OH)$_2$/NF in terms of HER specific activity, indicating that NiSe$_2$/Ni$_3$Se$_4$/NF-4 may have an inherent HER activity higher than NiSe$_2$/Ni$_3$Se$_4$/NF-1 and Ni(OH)$_2$/NF. The HER catalytic kinetics was also investigated through the electrochemical impedance spectroscopy (EIS) technique (Fig. S7b). The Nyquist plots of all catalysts exhibit a semicircle in the low-frequency range, which indexes the charge-transfer resistance of the catalysts. NiSe$_2$/Ni$_3$Se$_4$/NF-4 gives rise to a significantly smaller resistance (10 Ω) than that of NiSe$_2$/Ni$_3$Se$_4$/NF-1 (87 Ω), suggesting an intrinsic fast charge transfer of NiSe$_2$/Ni$_3$Se$_4$/NF-4 that can result in higher HER catalytic activity. The durability of NiSe$_2$/Ni$_3$Se$_4$/NF-4 was firstly evaluated by the chronoamperometric response at a constant potential of −0.177 V (vs RHE). As shown in Fig. 4d, the current density performs stable with negligible degradation during the 60 h test. Fig. S7c shows the multi-step chronopotentiometric curve of NiSe$_2$/Ni$_3$Se$_4$/NF-4 with current density at 10, 30, 50, 100, and 150 mA cm^{-2} for HER. The potential gives a response to the current density immediately and remains stable for each 1000 s, confirming the good stability of NiSe$_2$/Ni$_3$Se$_4$/NF-4. The inset of Fig. 4d shows the overpotential at 100 mA cm^{-2} shifts by only 13 mV after 2000 CV cycles, demonstrating high HER durability in 1.0 M KOH solution. We further characterize the elemental state and the phase

composition of the NiSe$_2$/Ni$_3$Se$_4$/NF-4 catalyst after the HER test. The XPS spectra of the post-HER catalyst (Fig. S8a) are almost equal to those of the pristine sample except for an increased Se-O amount, which could be ascribed to the surface oxidation of Se in strong alkaline electrolytes [40]. The XRD patterns of the post-HER catalyst nearly keep the initial reflections (Fig. S8c). The observations confirm the structural stability of NiSe$_2$/Ni$_3$Se$_4$/NF-4 during the HER test.

The sluggish OER process is the bottleneck of the overall water-splitting because it involves the four proton-coupled electron transfer pathways and the oxygen–oxygen bonding formation. The OER activities of NiSe$_2$/Ni$_3$Se$_4$/NF-1 and NiSe$_2$/Ni$_3$Se$_4$/NF-4 were determined via a three-electrode configuration in a 1.0 M KOH solution at a scan rate of 2 mV s^{-1}. For comparison, the Ni(OH)$_2$/NF, RuO$_2$ loaded on the NF, and bare NF electrodes were also measured to assess their OER performance. Polarization curves in Fig. 5a demonstrate that NiSe$_2$/Ni$_3$Se$_4$/NF-1 shows a much higher current density and lower overpotential at 100 mA cm^{-2} than Ni(OH)$_2$/NF, RuO$_2$ loaded on the NF, and NiSe$_2$/Ni$_3$Se$_4$/NF-1. The anodic peak near 1.4 V is originated from the oxidation of Ni^{2+} to Ni^{3+} [41]. NiSe$_2$/Ni$_3$Se$_4$/NF-1 delivers the markedly increased current density beyond 1.51 V (vs RHE). The overpotential to acquire a 100 mA cm^{-2} current density is only 309 mV, which is much
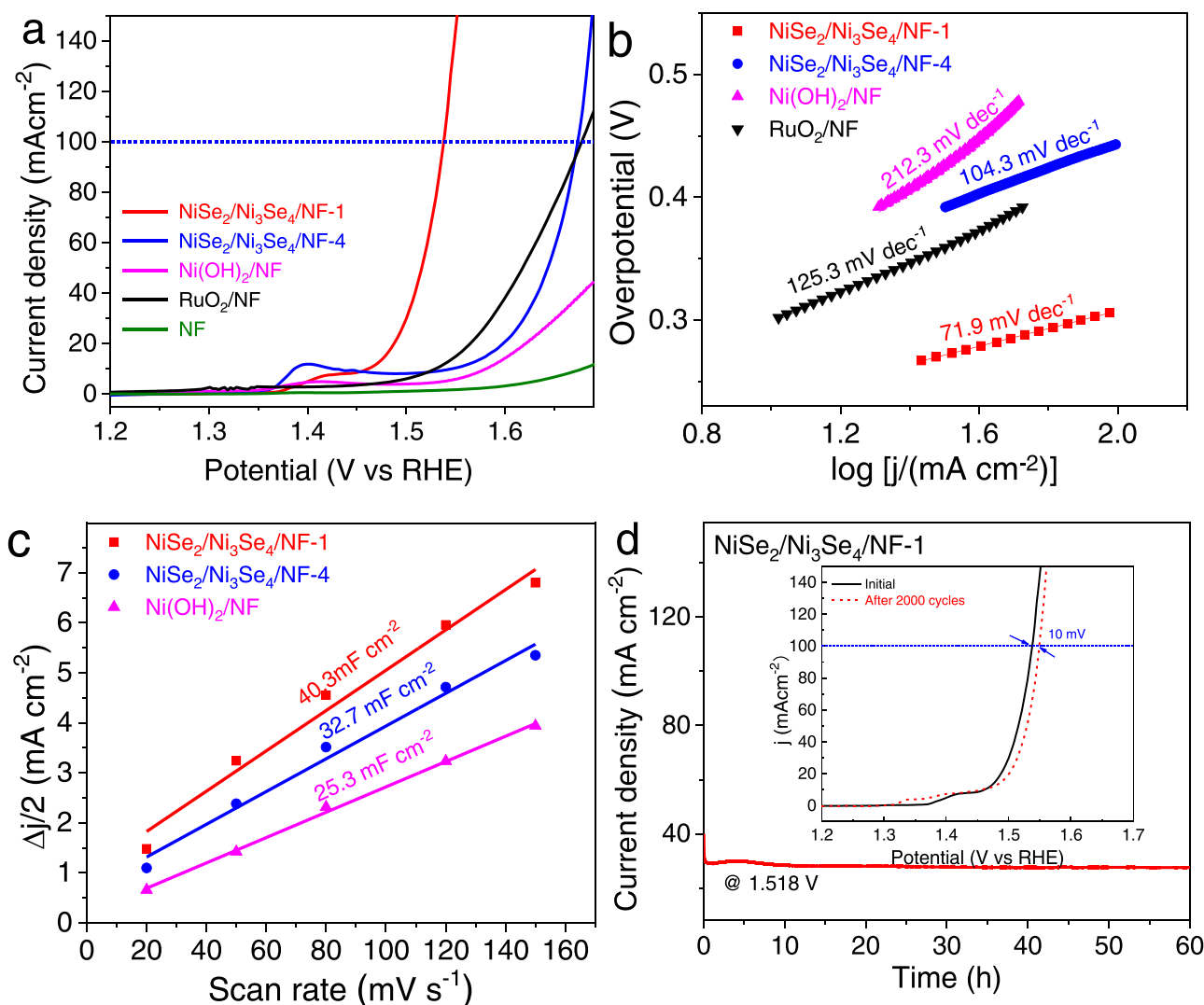
Fig. 5. (a) Polarization curves of NiSe$_2$/Ni$_3$Se$_4$/NF-1, NiSe$_2$/Ni$_3$Se$_4$/NF-4, Ni(OH)$_2$/NF, RuO$_2$/NF, and bare NF were performed at a scan rate of 2 mV s^{-1} for the OER. (b) The corresponding Tafel plots. (c) The capacitive current difference at 0.999 V (vs RHE) plotted against the scan rate for the assessment of the double-layer capacitance. (d) The chronoamperometric curve for NiSe$_2$/Ni$_3$Se$_4$/NF-1 at a constant potential of 1.518 V (vs RHE) for 60 h without iR correction. Inset: Polarization curves of the initial and after 2000 CV cycles for NiSe$_2$/Ni$_3$Se$_4$/NF-1 with iR correction.

Fig. 6. (a) LSV curves and the digital photo of the $NiSe_2/Ni_3Se_4/NF-1||NiSe_2/Ni_3Se_4/NF-4$ electrolyzer in 1.0 M KOH at a scan rate of 2 mV s^{-1}. (b) Chronopotentiometric curve of water electrolysis for this electrolyzer at a constant potential of 1.56 V for 12 h.

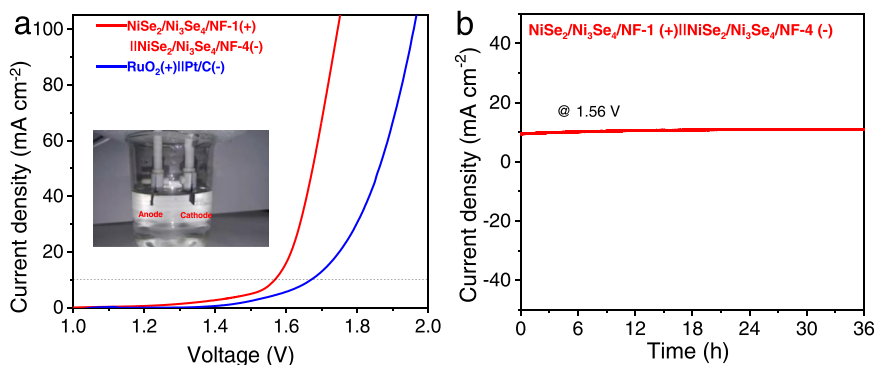lower than those for $NiSe_2/Ni_3Se_4/NF-4$ (444 mV) and RuO_2 (448 mV). The OER potential for $NiSe_2/Ni_3Se_4/NF-1$ at this large current density is also smaller than those for most active non-noble metal-based electrocatalysts, such as CuCoO-NWs (340 mV) [42], Ni_3C/C (390 mV) [43], Ni_3FeN-NPs (415 mV) [44], and other reported electrocatalysts (Table S2), indexing a potential practical value of this catalyst. The Tafel plot in Fig. 5b exhibits that the Tafel slope of $NiSe_2/Ni_3Se_4/NF-1$ is 71.9 mV dec^{-1}, which is lower than those of $NiSe_2/Ni_3Se_4/NF-4$ (104.3 mV dec^{-1}), RuO_2 on NF (125.3 mV dec^{-1}), and $Ni(OH)_2/NF$ (212.3 mV dec^{-1}), implying a beneficial OER kinetics for the $NiSe_2/Ni_3Se_4/NF-1$ electrode. The smaller Tafel slope reveals that this catalyst has a favorable affinity for OH$^-$ intermediates and can boost their formation and equilibrium electrosorption. Hence the succeeding oxygen evolution step will be rate-determining and results in a lower Tafel slope [3]. The ECSA values of the aforementioned catalysts are also determined by the C_{dl} method in the potential range from 0.924 to 1.074 V (vs RHE) since the oxidation of the selenides probably brings out the surface change during the OER (Fig. S9) [45,46]. Fig. 5c displays that the C_{dl} of $NiSe_2/Ni_3Se_4/NF-1$ is 40.3 mF cm^{-2}, which is distinctly larger than those for $NiSe_2/Ni_3Se_4/NF-4$ (32.7 mF cm^{-2}) and $Ni(OH)_2/NF$ (25.3 mF cm^{-2}). Even after normalization with ECSA, the OER specific activity of $NiSe_2/Ni_3Se_4/NF-1$ is distinctly superior to those for $NiSe_2/Ni_3Se_4/NF-4$ and $Ni(OH)_2/NF$, implying that $NiSe_2/Ni_3Se_4/NF-1$ may have a better intrinsic OER activity than $NiSe_2/Ni_3Se_4/NF-4$ and $Ni(OH)_2/NF$. These results reveal that $NiSe_2/Ni_3Se_4/NF-1$ possesses a large surface active area with more available active centers, which would guarantee its better OER performance.

In addition to the high OER activity, $NiSe_2/Ni_3Se_4/NF-1$ also shows good long-term stability. The chronoamperometric curve tested under a constant potential of 1.518 V (vs RHE) exhibits that the current response undergoes insignificant degradation during the continuous 60 h operation (Fig. 5d). The multi-step chronopotentiometric curve of $NiSe_2/Ni_3Se_4/NF-1$ is determined at different current densities of 30, 50, 100, 150, and 200 mA cm^{-2} for OER as shown in Fig. S10. It can be found that the potential signal shows the ultrafast response to each current density and keeps invariable for each time region. Inset in Fig. 5d exhibits that the LSV curve after 2000 CV cycles almost coincides with the initial one except for a small shift for the peak of the oxidation of Ni^{2+} to Ni^{3+} and a 10 mV positive shift of the overpotential at 100 mA cm^{-2}. The results suggest the good OER stability of $NiSe_2/Ni_3Se_4/NF-1$ in alkaline electrolytes. After the OER test, the morphologic and structural change of the catalyst is also analyzed by SEM, XPS, and XRD. As illustrated in Fig. S11, the SEM image reveals that large lamellar structures became less, while more small flakes were observed. Such a morphological change can be ascribed to the impact of evolving oxygen bubbles, which could strike or squeeze the nickel selenide nanosheets and modify the surface morphology of the catalyst. Ni 2p XPS spectrum exhibits that Ni^{2+} species were almost transformed into the high valent Ni^{3+} form, which is verified by two single peaks at 855.5 and 873.0 eV

compared to the original sample (Fig. S8b). The increased Ni^{3+} species is favorable for the OER performance and results in good durability due to the distinct positive shifts in binding energy, which are probably caused by the surface phase transition delocalizing the electron's intensity around metal atoms [47]. We do not find any signal of the NiOOH phase, which was reported at ~858 eV with a satellite peak at ~864 eV [26]. The XRD pattern reveals that the $NiSe_2$ phase in the post-OER catalyst had significantly converted to Ni_3Se_4 in the oxidative atmosphere (Fig. S8d), which commonly occurs for all-metal selenide electrocatalysts [48]. This transformation indirectly proves that the stable OER active component is Ni_3Se_4 rather than NiOOH in this catalyst [49]. Swesi's work has confirmed that nickel selenide is the active phase even after a prolonged OER test in an alkaline medium [50]. Although Ni-selenides have been reported as precatalysts, surfaces of which could be hydrolyzed to yield the true catalytically active phase of NiOOH for OER [45,51], surface hydrolysis and thorough conversion to a NiOOH overlayer involve the replacement of all the surface selenium anions with O/OH anions. According to Fajan's rule [52], the Ni−Se bond has higher bond strength than the Ni-O bond. This substitution is thus extremely difficult because of its high energy-intensive process especially at ambient temperature and at low applied potential [53].

Given the positive catalytic activities of $NiSe_2/Ni_3Se_4/NF-1$ for OER and $NiSe_2/Ni_3Se_4/NF-4$ for HER in an alkaline solution, a two-electrode electrolyzer in 1.0 M KOH was assembled by respectively employing the $NiSe_2/Ni_3Se_4/NF-1$ and $NiSe_2/Ni_3Se_4/NF-4$ catalysts as the anode and cathode of the overall water-splitting system (named as $NiSe_2/Ni_3Se_4/NF-1//NiSe_2/Ni_3Se_4/NF-4$). RuO_2 and Pt/C loaded on NF denoted as $RuO_2//Pt/C$ was also determined for comparison. As shown in Fig. 6a, the $NiSe_2/Ni_3Se_4/NF-1//NiSe_2/Ni_3Se_4/NF-4$ electrolyzer exhibits better electrocatalytic performance than $RuO_2//Pt/C$. The potential delivering a current density of 10 mA cm^{-2} for the former is 1.56 V, which is much lower than that for the latter (1.67 V). The hydrogen production efficiency was determined by a simply equipped set-up as shown in Fig. S12a. By using the 0.5×0.5 cm^2 catalyst electrode, the volumes of the produced hydrogen are collected as 5.2 and 10.5 ml after 30 and 60 min (Fig. S12b), respectively. The stability of the $NiSe_2/Ni_3Se_4/NF-1//NiSe_2/Ni_3Se_4/NF-4$ cell was assessed in 1.0 M KOH at a constant potential of 1.56 V (Fig. 6b). This system displays considerably high stability during a continuous 36 h process. To evaluate the electrode after testing, we determined the Ni^{2+} concentration in the electrolyte after the stability test. The ICP-AES result of Ni^{2+} content is 7.52×10^{-5} g/L, indicating that the $NiSe_2/Ni_3Se_4/NF$ catalysts are almost not dissolved in the 1.0 M KOH electrolyte. The trace catalyst residue was observed in the electrolyte after the 36 h testing (Fig. S13), revealing a slight peeling of the catalyst during the long-term stability test. However, in this work, the loss of the catalyst is less than 1 mg compared with the pristine loading of 7.4 ± 0.3 mg, indicating its good stability for overall water-splitting.
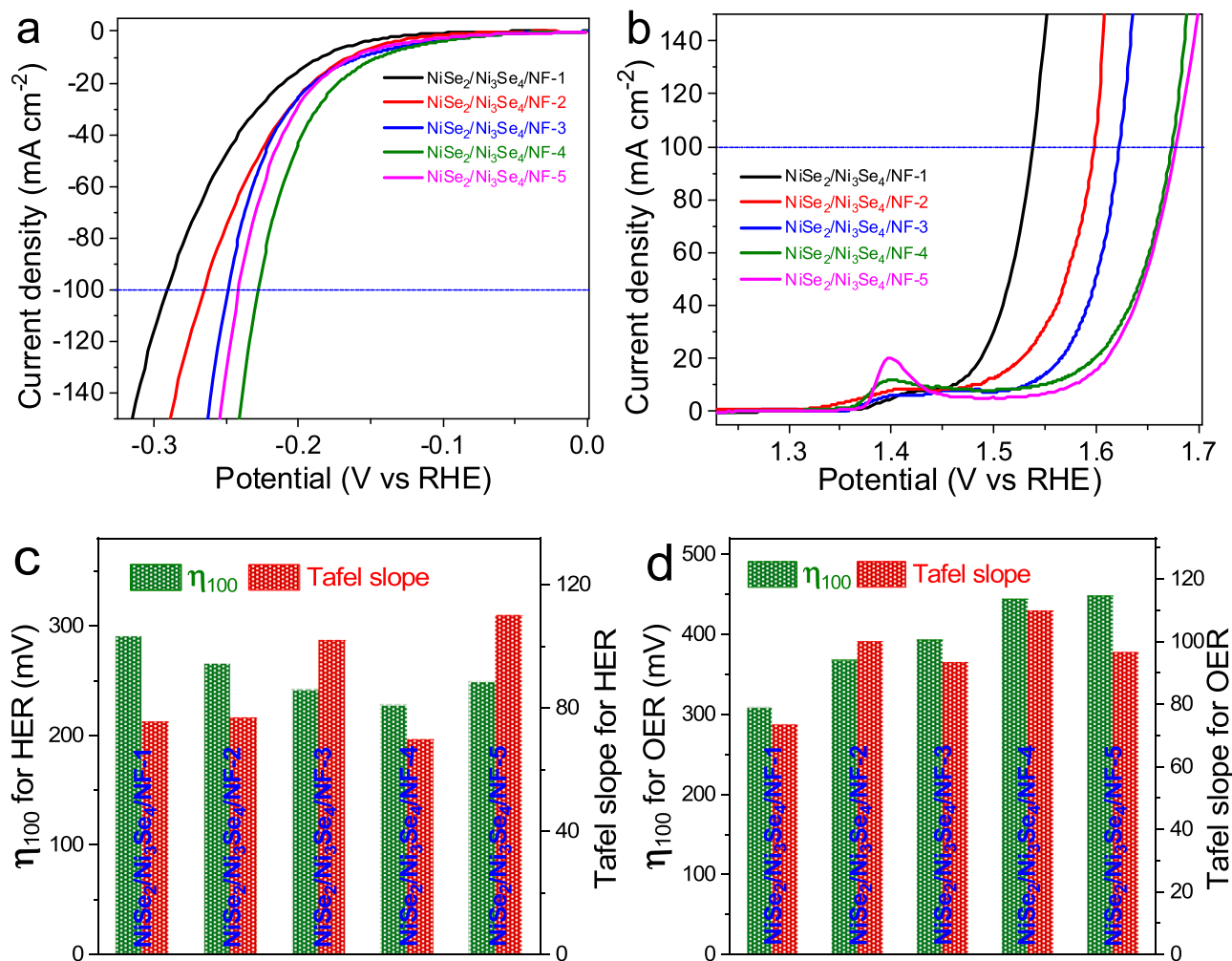
Fig. 7. HER (a) and OER (b) polarization curves of the series of NiSe$_2$/Ni$_3$Se$_4$/NF catalysts. Histograms of η_{100} and Tafel slope of HER (c) and OER (d) for the series of NiSe$_2$/Ni$_3$Se$_4$/NF.

3.3. Catalytic mechanism

Catalytic mechanism of electrocatalysts was investigated using a series of nickel selenide electrodes including NiSe$_2$/Ni$_3$Se$_4$/NF-1, NiSe$_2$/Ni$_3$Se$_4$/NF-2, NiSe$_2$/Ni$_3$Se$_4$/NF-3, NiSe$_2$/Ni$_3$Se$_4$/NF-4, and NiSe$_2$/Ni$_3$Se$_4$/NF-5. Their HER and OER activities in 1.0 M KOH were systematically studied. Fig. 7a exhibits the HER electrocatalytic performance gradually ameliorates with increasing the Se powder except for NiSe$_2$/Ni$_3$Se$_4$/NF-5, which shows the slightly inferior activity to NiSe$_2$/Ni$_3$Se$_4$/NF-4 since the excess Se would mask some active sites of the catalyst. HER overpotentials of NiSe$_2$/Ni$_3$Se$_4$/NF electrodes to reach the current density of 100 mA cm^{-2} decreases from NiSe$_2$/Ni$_3$Se$_4$/NF-1 to NiSe$_2$/Ni$_3$Se$_4$/NF-4 and increases from NiSe$_2$/Ni$_3$Se$_4$/NF-4 to NiSe$_2$/Ni$_3$Se$_4$/NF-5. Their specific activities based on ESCA almost follow a similar situation (Fig. S14a). Their corresponding Tafel slopes show a similar tendency (Fig. 7c). Conversely, the OER electrocatalytic performance slowly deteriorates from NiSe$_2$/Ni$_3$Se$_4$/NF-1 to NiSe$_2$/Ni$_3$Se$_4$/NF-4, whose activity is nearly equal to that for NiSe$_2$/Ni$_3$Se$_4$/NF-5 (Fig. 7b). This trend in OER performance is also confirmed by their overpotentials, Tafel slopes (Fig. 7d), and specific activities (Fig. S14b). It should be emphasized that both HER and OER activities of any NiSe$_2$/Ni$_3$Se$_4$/NF catalyst electrode are superior to those for the pure-phase NiSe$_2$/NF or Ni$_3$Se$_4$/NF catalyst (Fig. S15), indicating the favorable synergistic effects in the dual-phase catalyst.

It is well accepted that introducing metal cations in a higher oxidation state in electrocatalysts could facilitate OER, during which metal species would be oxidized to highly oxidative forms before the onset of the reaction [54]. These high-valent metal ions are recognized as the real electrocatalytic centers. XPS analysis results from Fig. 2b illustrate that NiSe$_2$/Ni$_3$Se$_4$/NF-1 has a higher relative mole ratio of Ni^{3+}/Ni^{2+} (1.442) than NiSe$_2$/Ni$_3$Se$_4$/NF-4 (1.125), revealing higher content of highly oxidative Ni species in NiSe$_2$/Ni$_3$Se$_4$/NF-1. This observation is highly consistent with the semi-quantitative results of their XRD patterns by using the Highscore software (Fig. S4). These highly oxidized Ni species ensure the superior OER performance of NiSe$_2$/Ni$_3$Se$_4$/NF-1 to NiSe$_2$/Ni$_3$Se$_4$/NF-4. The OER mechanism for transition metal electrocatalysts can be elucidated by the following four steps [55]: (1) $* + OH^- \rightarrow *OH + e^-$; (2) $*OH + OH- \rightarrow H_2O + *O + e^-$; (3) $*O + OH^-$ $*OOH + e^-$; (4) $*OOH + OH^- \rightarrow * + O_2 + e^-$. The third step for the formation of the *OOH intermediate is the key step in OER [3]. The more high-valence Ni species in the selenides can promote electrostatic adsorption of OH$^-$ ions, and thus NiSe$_2$/Ni$_3$Se$_4$/NF-1 brings out the much better OER electrocatalytic performance than NiSe$_2$/Ni$_3$Se$_4$/NF-4 due to its higher Ni^{3+}/Ni^{2+} ratio. Besides, the localized negative charges on Se active centers (Se$^{\delta-}$) can deactivate electrocatalysts from coordinating with the OH$^-$ group, which may considerably impair the OER catalytic performance [12]. Therefore, NiSe$_2$/Ni$_3$Se$_4$/NF-1 containing less Se$^{\delta-}$ species displays a much larger current density, lower overpotential at 100 mA cm^{-2}, and smaller Tafel slope than NiSe$_2$/Ni$_3$Se$_4$/NF-4 for OER system.
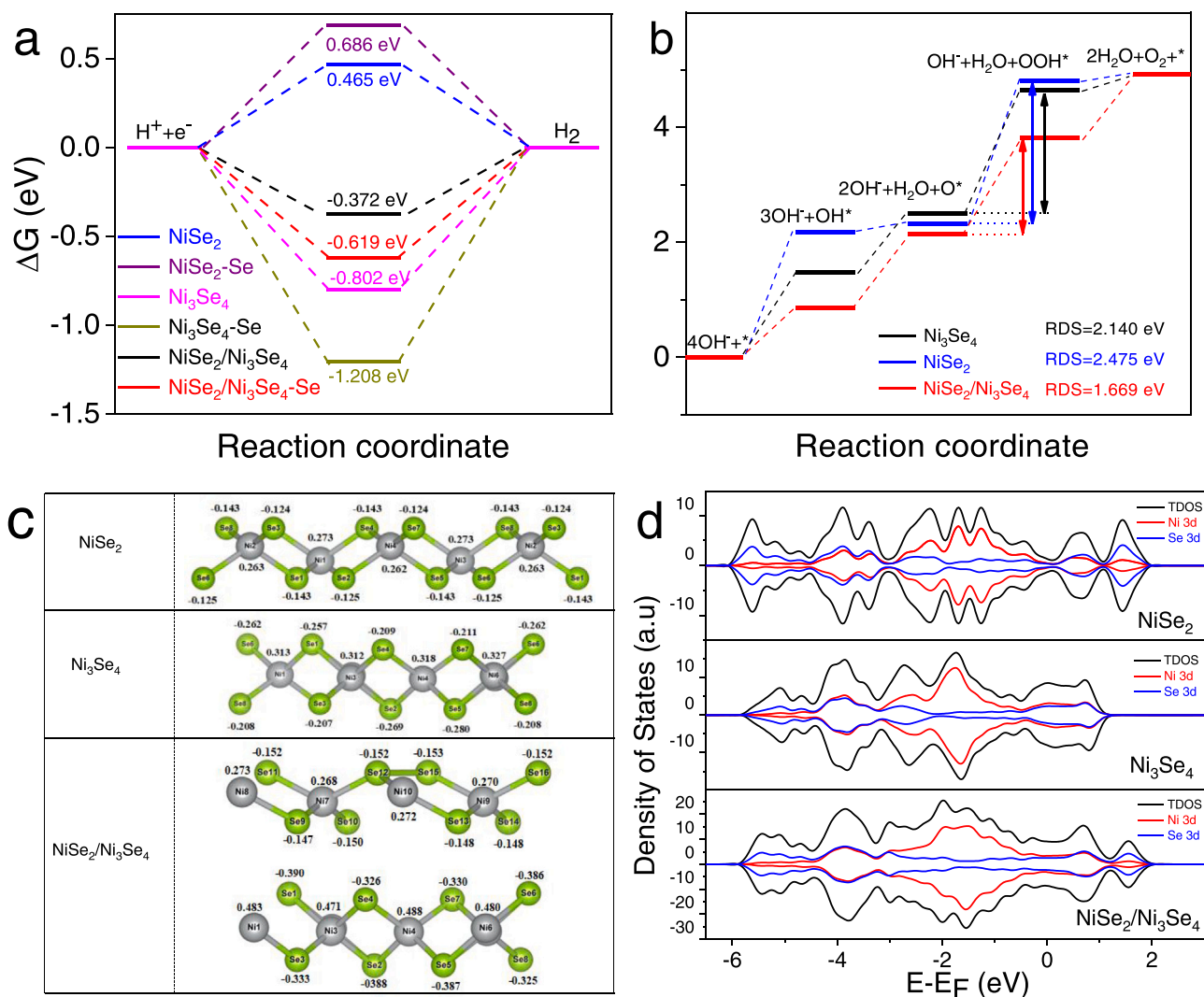
Fig. 8. (a, b) The standard free energy diagrams in the HER and OER process on $NiSe_2$, Ni_3Se_4, and $NiSe_2/Ni_3Se_4$ at U = 0. (c) The Bader charge numbers of atoms in $NiSe_2$, Ni_3Se_4, and $NiSe_2/Ni_3Se_4$ heterostructures (green: Se, and gray: Ni). (d) The density of states (DOS) on $NiSe_2$, Ni_3Se_4, and $NiSe_2/Ni_3Se_4$.

For HER, $NiSe_2/Ni_3Se_4/NF-4$ exhibits enhanced electrocatalytic performance, which can be ascribed to faster kinetics and a more rapid charge transfer based on analyses of the Tafel slope and EIS results (Figs. 7c and S7c). The $NiSe_2/Ni_3Se_4/NF-4$ electrode also has a larger ESCA and a better specific activity than $NiSe_2/Ni_3Se_4/NF-1$ (Figs. S6 and S7a). The high HER electrocatalytic activity of $NiSe_2/Ni_3Se_4/NF-4$ can also be attributed to more $Se^{\delta-}$ and less oxidative Ni species [12]. XPS spectra also reveal that the $NiSe_2/Ni_3Se_4/NF-4$ electrode with a smaller relative mole ratio of Ni^{3+}/Ni^{2+} has more $Se^{\delta-}$. It is supposed that the HER of five $NiSe_2/Ni_3Se_4/NF$ electrodes follows a Volmer ($H_2O + e^- \rightarrow H^* + OH^-$) –Heyrovsky ($H_2O + e^- + H^* \rightarrow H_2 + OH^-$) pathway in alkaline media since their Tafel slopes range from 40 to 120 mV dec^{-1} [56]. Such pathway involves adsorption of H_2O, electrochemical splitting of the captured H_2O into adsorbed H^* and OH^- species, desorption of OH^- to clean the catalyst's surface, and formation of H^* for H_2 generation. Therefore, the formation and desorption of OH^- might be significant for HER in alkaline conditions. Ni metal has an appropriate H atom binding energy close to Pt [57], but much lower HER catalytic activity than Pt. The generated OH^- could preferentially attach to the oxidized Ni site due to strong electrostatic affinity to the locally positively charged Ni cation species. Whereas $Se^{\delta-}$ active sites would promote the adsorption of the H^* intermediates because of the polarization induced partial negative charges localized on $Se^{\delta-}$ centers and the moderate Se–H bond strength (276 kJ mol^{-1}) [13,14]. Accordingly,

$NiSe_2/Ni_3Se_4/NF-4$ with a moderate number of $Se^{\delta-}$ sites presents the best HER electrocatalytic performance among all $NiSe_2/Ni_3Se_4/NF$ electrodes.

3.4. Density functional theory (DFT) calculations

DFT calculations were additionally implemented for a further investigation of the catalytic activity for HER and OER in alkaline media. For the HER process, the inherent activity of electrocatalysts can be generally evaluated by the Gibbs free energy of hydrogen adsorption (ΔG_{H^*}), which is a critical indicator for the adsorption and desorption efficiency of H^* [58]. Hence, the ΔG_{H^*} values of $NiSe_2$, Ni_3Se_4, and $NiSe_2/Ni_3Se_4$ were first calculated as shown in Fig. 8a, and the theoretical models of $NiSe_2/Ni_3Se_4$, $NiSe_2$, and Ni_3Se_4 are presented in Figs. S16–S23. The ΔG_{H^*} value of the Ni site in $NiSe_2/Ni_3Se_4$ is obtained as −0.372 eV, which is the closest to the ideal state of 0 eV and outperforms other counterparts such as $NiSe_2$ (Ni site, 0.465 eV), $NiSe_2$ (Se site, 0.686 eV), Ni_3Se_4 (Ni site, −0.802 eV), Ni_3Se_4 (Se site, −1.208 eV), and $NiSe_2/Ni_3Se_4$ (Se site, −0.619 eV). The above data also disclose that the Ni site in all catalysts is the real HER active site and $NiSe_2$ possesses the superior HER activity to Ni_3Se_4, which is highly matched with the electrochemical results. We also computed the OER ΔG profiles on the surfaces of $NiSe_2$, Ni_3Se_4, and $NiSe_2/Ni_3Se_4$ models (only Ni site) at U = 0 V by following the aforementioned four-step electron transfer

process under alkaline conditions [54]. According to the diagrams in Fig. 8b and Figs. S24–S26, their rate-determining step (RDS) appears at the third step for the oxidation of *O to *OOH species in the OER process on NiSe$_2$, Ni$_3$Se$_4$, and NiSe$_2$/Ni$_3$Se$_4$. The NiSe$_2$/Ni$_3$Se$_4$ catalyst affords a much smaller uphill ΔG of 1.669 eV than the single-phase Ni$_3$Se$_4$ (2.140 eV) and NiSe$_2$ (2.475 eV), which also reveals that Ni$_3$Se$_4$ owns the better OER activity than NiSe$_2$. Considering the better HER activity of NiSe$_2$ and OER activity of Ni$_3$Se$_4$, it is reasonably found that NiSe$_2$/Ni$_3$Se$_4$/NF-4 displays the better HER performance and NiSe$_2$/-Ni$_3$Se$_4$/NF-1 exhibits the better OER performance. The charge density difference shows that the electron accumulates near the NiSe$_2$ side, indicating an electronic migration from Ni$_3$Se$_4$ to NiSe$_2$ (Fig. S16b). The Bader charges (q) analysis of the local atoms on NiSe$_2$, Ni$_3$Se$_4$, and NiSe$_2$/Ni$_3$Se$_4$ also supports this phenomenon. As presented in Fig. 8c, the q values of Ni atoms increase at the heterointerface on the Ni$_3$Se$_4$ side but decrease at the NiSe$_2$ side compared with the pure Ni$_3$Se$_4$ and NiSe$_2$ phase, further suggesting the electron transfer from Ni$_3$Se$_4$ to NiSe$_2$ at the heterointerface on NiSe$_2$/Ni$_3$Se$_4$. Consequently, the accumulative electrons on the NiSe$_2$ side result in increased positive charges on the Ni$_3$Se$_4$ surface through the redistribution of interfacial charge. In other words, NiSe$_2$ with increased negative charges could accelerate the adsorption of H* species [59], and Ni$_3$Se$_4$ with increased positive charges could facilitate the adsorption of oxygen-containing intermediates (OH$^-$ and OOH) [60] in the dual-phase electrocatalysts. This interfacial charge transfer also supports the fact that NiSe$_2$/Ni$_3$Se$_4$/NF-4 displays a better HER activity and NiSe$_2$/Ni$_3$Se$_4$/NF-1 exhibits a better OER activity since the former contains more NiSe$_2$ phases but the latter possesses more Ni$_3$Se$_4$ components. Besides, we also calculated the density of the states (DOS), which can index the electrical conductivity of heterostructure. The DOS results in Fig. 8d demonstrate that NiSe$_2$/Ni$_3$Se$_4$ exhibits a higher carrier density near the Fermi level than NiSe$_2$ and Ni$_3$Se$_4$, implying a promising electrocatalyst. These results explicitly reveal that the strong interaction between NiSe$_2$ and Ni$_3$Se$_4$ could modulate the interfacial electronic structures of the dual-phase catalyst for the enhanced electrocatalytic activity.

4. Conclusion

Summarily, we have developed a simple and facile method for the in situ preparation of new dual-phase nickel selenide electrodes containing NiSe$_2$ and Ni$_3$Se$_4$ phases on nickel foam. The phase composition and charge state of Ni species are manipulated by simply controlling the mass ratio of raw materials. The as-obtained dual-phase electrode exhibits promising catalytic activity toward both the HER and the OER in 1.0 M KOH. However, the HER and OER electrocatalytic activities are highly dependent on their phase composition and charge state. NiSe$_2$/Ni$_3$Se$_4$/NF-4 containing more NiSe$_2$ phase displays the best HER activity while NiSe$_2$/Ni$_3$Se$_4$/NF-1 containing more Ni$_3$Se$_4$ phase shows the best HER activity. Their prominent and stable electrocatalytic performances are mainly assigned to the following two aspects. (i) In situ growth of 3D NiSe$_2$/Ni$_3$Se$_4$ heterostructure assembled on NF guarantees intimate integration, good electrical conductivity, more accessible active sites, rapid charge transfer, mass transport, and gaseous products release, which thus result in good catalytic activity and durability. (ii) The experimental characterizations and DFT calculations disclose that the interfacial electronic redistribution on NiSe$_2$/Ni$_3$Se$_4$ increases electrical conductivity and decreases the barriers of adsorption and desorption energy. Due to these advantages, the corresponding electrolyzer using NiSe$_2$/Ni$_3$Se$_4$/NF-4 and NiSe$_2$/Ni$_3$Se$_4$/NF-1 as the respective cathode and anode delivers the current density of 10 mA cm^{-2} at a low voltage of 1.56 V along with good durability. This study offers a novel avenue for the fabrication of nickel selenide electrocatalysts with improved electrocatalytic activity and identifies this dual-phase hybrid as a promising candidate for water-splitting.

CRediT authorship contribution statement

Lei Tan: Investigation, Methodology, Data curation, Software, Writing – original draft. **Jiangtao Yu:** Data curation, Software, Writing – original draft. **Haiyan Wang:** Data curation, Investigation. **Hongtao Gao:** Validation, Supervision. **Xien Liu:** Writing – review & editing. **Lei Wang:** Validation, Supervision. **Xilin She:** Supervision. **Tianrong Zhan:** Methodology, Project administration, Writing – review & editing.

Declaration of Competing Interest

The authors declare that they have no known competing financial interests or personal relationships that could have appeared to influence the work reported in this paper.

Appendix A. Supporting information

Supplementary data associated with this article can be found in the online version at doi:10.1016/j.apcatb.2021.120915.

References

[1] Y. Zheng, Y. Jiao, Y. Zhu, L. Li, Y. Han, Y. Chen, A. Du, M. Jaroniec, S. Qiao, Hydrogen evolution by a metal-free electrocatalyst, Nat. Commun. 5 (2014) 3783.

[2] W. Ma, R. Ma, C. Wang, J. Liang, X. Liu, K. Zhou, T. Sasaki, A superlattice of alternately stacked Ni-Fe hydroxide nanosheets and graphene for efficient splitting of water, ACS Nano 9 (2015) 1977–1984.

[3] Y. Jiao, Y. Zheng, M. Jaroniec, S. Qiao, Design of electrocatalysts for oxygen- and hydrogen-involving energy conversion reactions, Chem. Soc. Rev. 44 (2015) 2060–2086.

[4] H. Qi, P. Zhang, H. Wang, Y. Cui, X. Liu, X. She, Y. Wen, T. Zhan, Cu$_2$Se nanowires shelled with NiFe layered double hydroxide nanosheets for overall water-splitting, J. Colloid Interface Sci. 599 (2021) 370–380.

[5] Y. Guo, T. Park, J. Yi, J. Henzie, J. Kim, Z. Wang, B. Jiang, Y. Bando, Y. Sugahara, J. Tang, Y. Yamauchi, Nanoarchitectonics for transition-metal-sulfide-based electrocatalysts for water splitting, Adv. Mater. 31 (2019), 1807134.

[6] D. Esposito, S. Hunt, Y. Kimmel, J. Chen, A new class of electrocatalysts for hydrogen production from water electrolysis: metal monolayers supported on low-cost transition metal carbides, J. Am. Chem. Soc. 134 (2012) 3025–3033.

[7] G. Wang, W. Chen, G. Chen, J. Huang, C. Song, D. Chen, Y. Du, C. Li, K. Ostrikov, Trimetallic Mo–Ni–Co selenides nanorod electrocatalysts for highly-efficient and ultra-stable hydrogen evolution, Nano Energy 71 (2020), 104637.

[8] Z. Chen, Z. Hzong, W. Hu, H. Yin, G. Cao, H. Wen, J. Wang, P. Wang, Highly dispersed Ni$_{2-x}$Mo$_x$P nanoparticles on oxygen-defect-rich NiMoO$_{4-y}$ nanosheets as an active electrocatalyst for alkaline hydrogen evolution reaction, J. Power Sources 444 (2019), 227311.

[9] T. Zhan, Y. Sun, Y. Wang, W. Cao, X. Liu, H. Teng, W. Hou, In situ growth of ultrathin NiFe layered double hydroxide nanosheets on reduced oxide graphene as an enhanced oxygen evolution electrocatalyst, J. Colloid Interface Sci. 552 (2019) 671–677.

[10] T. Zhan, X. Liu, S. Lu, W. Hou, Nitrogen doped NiFe layered double hydroxide/ reduced graphene oxide mesoporous nanosphere as an effective bifunctional electrocatalyst for oxygen reduction and evolution reactions, Appl. Catal. B Environ. 205 (2017) 551–558.

[11] W. Hong, M. Risch, K. Stoerzinger, A. Grimaud, J. Suntivich, Y. Shao-Horn, Toward the rational design of non-precious transition metal oxides for oxygen electrocatalysis, Energy Environ. Sci. 8 (2015) 1404–1427.

[12] S. Anantharaj, S. Ede, K. Sakthikumar, K. Karthick, S. Mishra, S. Kundu, Recent trends and perspectives in electrochemical water splitting with an emphasis on sulfide, selenide, and phosphide catalysts of Fe, Co, and Ni: a review, ACS Catal. 6 (2016) 8069–8097.

[13] J. Hu, C. Zhang, X. Meng, H. Lin, C. Hu, X. Long, S. Yang, Hydrogen evolution electrocatalysis with binary-nonmetal transition metal compounds, J. Mater. Chem. A 5 (2017) 5995–6012.

[14] P. Ramakrishnan, S. Jo, N. Pitipuech, J. Sohn, Bifunctionality behavior of phase controlled nickel selenides in alkaline water electrolysis application, Electrochim. Acta 354 (2020), 136742.

[15] M. Gao, Z. Lin, T. Zhuang, J. Jiang, Y. Xu, Y. Zheng, S. Yu, Mixed-solution synthesis of sea urchin-like NiSe nanofiber assemblies as economical Pt-free catalysts for electrochemical H_2 production, J. Mater. Chem. 22 (2012) 13662–13668.

[16] C. McCarthy, C. Downes, R. Brutchey, Room temperature dissolution of bulk elemental Ni and Se for solution deposition of a $NiSe_2$ HER electrocatalyst, Inorg. Chem. 56 (2017) 10143–10146.

[17] M. Nath, J. Masud, A. Swesi, T. Energy, E. Ees, Nickel selenide as a high-efficiency catalyst for oxygen evolution reaction, Energy Environ. Sci. 9 (2016) 1771–1782.

[18] K. Xu, H. Ding, H. Lv, S. Tao, P. Chen, X. Wu, W. Chu, C. Wu, Y. Xie, Understanding structure-dependent catalytic performance of nickel selenides for electrochemical water oxidation, ACS Catal. 7 (2017) 310–315.

[19] S. Wang, P. He, L. Jia, M. He, T. Zhang, F. Dong, M. Liu, H. Liu, Y. Zhang, C. Li, J. Gao, L. Bian, Nanocoral-like composite of nickel selenide nanoparticles anchored on two-dimensional multi-layered graphitic carbon nitride: A highly efficient electrocatalyst for oxygen evolution reaction, Appl. Catal. B Environ. 243 (2019) 463–469.

[20] S. Ananthataj, E. Subhashini, K.C. Swaathini, T.S. Amarnath, S. Chatterjee, K. Karthick, S. Kundu, Respective influence of stoichiometry and NiOOH formation in hydrogen and oxygen evolution reactions of nickel selenides, Appl. Surf. Sci. 487 (2019) 1152–1158.

[21] J. Shi, J. Hu, Y. Luo, X. Sun, A. Asiri, Ni_3Se_2 film as a non-precious metal bifunctional electrocatalyst for efficient water splitting, Catal. Sci. Technol. 5 (2015) 4954–4958.

[22] S. Ananthataj, J. Kennedy, S. Kundu, Microwave-initiated facile formation of Ni_3Se_4 nanoassemblies for enhanced and stable water splitting in neutral and alkaline media, ACS Appl. Mater. Interfaces 9 (2017) 8714–8728.

[23] S. Jin, Are metal chalcogenides, nitrides, and phosphides oxygen evolution catalysts or bifunctional catalysts? ACS Energy Lett. 2 (2017) 1937–1938.

[24] F. Zhang, Y. Pei, Y. Ge, H. Chu, S. Craig, P. Dong, J. Cao, P. Ajayan, M. Ye, J. Shen, Controlled synthesis of eutectic $NiSe/Ni_3Se_2$ self-supported on Ni foam: an excellent bifunctional electrocatalyst for overall water splitting, Adv. Mater. Interfaces 5 (2018), 1701507.

[25] P. Liu, L. Zhang, L. Zheng, H. Yang, Surface engineering of nickel selenide for an enhanced intrinsic overall water splitting ability, Mater. Chem. Front. 2 (2018) 1725–1731.

[26] F. Ming, H. Liang, H. Shi, X. Xu, G. Mei, Z. Wang, MOF-derived Co-doped nickel selenide/C electrocatalysts supported on Ni foam for overall water splitting, J. Mater. Chem. A 4 (2016) 15148–15155.

[27] J. Geisenhoff, A. Tamura, A. Schimpf, Manipulation of precursor reactivity for the facile synthesis of heterostructured and hollow metal selenide nanocrystals, Chem. Mater. 32 (2020) 2304–2312.

[28] Z. Huang, S. Yuan, T. Zhang, B. Cai, B. Xu, X. Lu, L. Fan, F. Dai, D. Sun, Selective selenization of mixed-linker Ni-MOFs: $NiSe_2$@NC core-shell nano-octahedrons with tunable interfacial electronic structure for hydrogen evolution reaction, Appl. Catal. B Environ. 272 (2020), 118976.

[29] X. Wang, W. Li, D. Xiong, D. Petrovykh, L. Liu, Bifunctional nickel phosphide nanocatalysts supported on carbon fiber paper for highly effi cient and stable overall water splitting, Adv. Funct. Mater. 26 (2016) 4067–4077.

[30] W. Zhang, C. Feng, H. Wu, L. Zhang, J. Zhang, Novel cobalt-doped $Ni_{0.85}Se$ chalcogenides ($Co_xNi_{0.85-x}Se$) as high active and stable electrocatalysts for hydrogen evolution reaction in electrolysis water splitting, ACS Appl. Mater. Interfaces 10 (2018) 40491–40499.

[31] M. Chauhan, K. Reddy, C. Gopinath, S. Deka, Copper cobalt sulfide nanosheets realizing a promising electrocatalytic oxygen evolution reaction, ACS Catal. 7 (2017) 5871–5879.

[32] Z. Xue, X. Li, Q. Liu, M. Cai, K. Liu, M. Liu, Z. Ke, X. Liu, G. Li, Interfacial electronic structure modulation of nite nanoarrays with NiS nanodots facilitates electrocatalytic oxygen evolution, Adv. Mater. 31 (2019), 1900430.

[33] D. Li, H. Baydoun, C. Verani, S. Brock, Efficient water oxidation using CoMnP nanoparticles, J. Am. Chem. Soc. 138 (2016) 4006–4009.

[34] G. Fang, Q. Wang, J. Zhou, Y. Lei, Z. Chen, Z. Wang, A. Pan, S. Liang, Metal organic framework-templated synthesis of bimetallic selenides with rich phase boundaries for sodium-ion storage and oxygen evolution reaction, ACS Nano 13 (2019) 5635–5645.

[35] Y. Yang, Y. Kang, H. Zhao, X. Dai, M. Cui, X. Luan, X. Zhang, F. Nie, Z. Ren, W. Song, An interfacial electron transfer on tetrahedral $NiS_2/NiSe_2$ heterocages with dual-phase synergy for efficiently triggering the oxygen evolution reaction, Small 16 (2020), 1905083.

[36] W. Li, B. Yu, Y. Hu, X. Wang, D. Yang, Y. Chen, Core-shell structure of $NiSe_2$ nanoparticles@nitrogen-doped graphene for hydrogen evolution reaction in both acidic and alkaline media, ACS Sustain. Chem. Eng. 7 (2019) 4351–4359.

[37] Y. Zhao, B. Jin, Y. Zheng, H. Jin, Y. Jiao, S. Qiao, Charge state manipulation of cobalt selenide catalyst for overall seawater electrolysis, Adv. Energy Mater. 8 (2018), 1801926.

[38] Z. Fang, L. Peng, Y. Qian, X. Zhang, Y. Xie, J. Cha, G. Yu, Dual tuning of Ni–Co–A (A = P, Se, O) nanosheets by anion substitution and holey engineering for efficient hydrogen evolution, J. Am. Chem. Soc. 140 (2018) 5241–5247.

[39] Z. Huang, Z. Chen, Z. Chen, C. Lv, M. Humphrey, C. Zhang, Cobalt phosphide nanorods as an efficient electrocatalyst for the hydrogen evolution reaction, Nano Energy 9 (2014) 373–382.

[40] D. Kong, H. Wang, Z. Lu, Y. Cui, $CoSe_2$ nanoparticles grown on carbon fiber paper: an efficient and stable electrocatalyst for hydrogen evolution reaction, J. Am. Chem. Soc. 136 (2014) 4897–4900.

[41] R. Xu, R. Wu, Y. Shi, J. Zhang, B. Zhang, Ni_3Se_2 nanoforest/Ni foam as a hydrophilic, metallic, and self-supported bifunctional electrocatalyst for both H_2 and O_2 generations, Nano Energy 24 (2016) 103–110.

[42] M. Kuang, P. Han, Q. Wang, J. Li, G. Zheng, CuCo hybrid oxides as bifunctional electrocatalyst for efficient water splitting, Adv. Funct. Mater. 26 (2016) 8555–8561.

[43] K. Xu, H. Ding, H. Lv, P. Chen, X. Lu, H. Cheng, T. Zhou, S. Liu, X. Wu, C. Wu, Y. Xie, Dual electrical-behavior regulation on electrocatalysts realizing enhanced electrochemical water oxidation, Adv. Mater. 28 (2016) 3326–3332.

[44] X. Jia, Y. Zhao, G. Chen, L. Shang, R. Shi, X. Kang, G. Waterhouse, L. Wu, C. Tung, T. Zhang, Ni_3FeN nanoparticles derived from ultrathin NiFe-layered double hydroxide nanosheets: an efficient overall water splitting electrocatalyst, Adv. Energy Mater. 6 (2016), 1502585.

[45] C. Tang, N. Cheng, Z. Pu, W. Xing, X. Sun, NiSe nanowire film supported on nickel foam: an efficient and stable 3D bifunctional electrode for full water splitting, Angew. Chem. Int. Ed. 54 (2015) 9351–9355.

[46] C. Xia, Q. Jiang, C. Zhao, M. Hedhili, H. Alshareef, Selenide-based electrocatalysts and scaffolds for water oxidation applications, Adv. Mater. 28 (2016) 77–85.

[47] J. Zhou, Y. Dou, T. He, A. Zhou, X. Kong, X. Wu, T. Liu, J. Li, Revealing the effect of anion-tuning in bimetallic chalcogenides on electrocatalytic overall water splitting, Nano Res. (2021), https://doi.org/10.1007/s12274-021-3370-7.

[48] S. Ananthataj, E. Subhashini, K. Swaathini, T. Amarnath, S. Chatterjee, K. Karthick, S. Kundu, Respective influence of stoichiometry and NiOOH formation in hydrogen and oxygen evolution reactions of nickel selenides, Appl. Surf. Sci. 487 (2019) 1152–1158.

[49] G. Liu, Z. Zhang, J. Li, J. Liu, X. Long, H. Chen, H. Tong, Z. Liu, D. Qian, Constructing heterostructured $CoSe_2/Ni_3Se_4$@N-doped carbon nanosheets/ketjen black carbon as a robust oxygen evolution electrocatalyst, Int. J. Hydrog. Energy 45 (2020) 30666–30672.

[50] A. Swesi, J. Masud, M. Nath, Nickel selenide as a high-efficiency catalyst for oxygen evolution reaction, Energy Environ. Sci. 9 (2016) 1771–1782.

[51] K. Xu, H. Ding, H. Lv, S. Tao, P. Chen, X. Wu, W. Chu, C. Wu, Y. Xie, Understanding structure-dependent catalytic performance of nickel selenides for electrochemical water oxidation, ACS Catal. 7 (2017) 310–315.

[52] G. Miessler, P. Fischer, D. Tarr. Inorganic Chemistry, fifth ed., Prentice Hall, 2014.

[53] S. De, J. See, W. Liyanage, J. Masud, J. Wu, W. Yang, W. Chen, D. Prendergast, M. Nath, Understanding the structural evolution of a nickel chalcogenide electrocatalyst surface for water oxidation, Energy Fuels 35 (2021) 4387–4403.

[54] C. Guo, Y. Zheng, J. Ran, F. Xie, M. Jaroniec, S. Qiao, Engineering high-energy interfacial structures for high-performance oxygen-involving electrocatalysis, Angew. Chem. Int. Ed. 56 (2017) 8539–8543.

[55] J. Nørskov, J. Rossmeisl, A. Logadottir, L. Lindqvist, J. Kitchin, T. Bligaard, H. Jónsson, Origin of the overpotential for oxygen reduction at a fuel-cell cathode, J. Phys. Chem. B 108 (2004) 17886–17892.

[56] Z. Huang, Z. Chen, Z. Chen, C. Lv, M. Humphrey, C. Zhang, Cobalt phosphide nanorods as an efficient electrocatalyst for the hydrogen evolution reaction, Nano Energy 9 (2014) 373–382.

[57] J. Greeley, T. Jaramillo, J. Bonde, I. Chorkendorff, J. Nørskov, Computational high-throughput screening of electrocatalytic materials for hydrogen evolution reaction, Nat. Mater. 5 (2006) 909–913.

[58] Z. Huang, S. Yuan, T. Zhang, B. Cai, B. Xu, X. Lu, L. Fan, F. Dai, D. Sun, Selective selenization of mixed-linker Ni-MOFs: $NiSe_2$@NC core-shell nano-octahedrons with tunable interfacial electronic structure for hydrogen evolution reaction, Appl. Catal. B Environ. 272 (2020), 118976.

[59] L. Yang, L. Huang, Y. Yao, L. Jiao, In-situ construction of lattice-matching $NiP_2/NiSe_2$ heterointerfaces with electron redistribution for boosting overall water splitting, Appl. Catal. B Environ. 282 (2021), 119584.

[60] G. Fang, Q. Wang, J. Zhou, Y. Lei, Z. Chen, Z. Wang, A. Pan, S. Liang, Metal organic framework-templated synthesis of bimetallic selenides with rich phase boundaries for sodium-ion storage and oxygen evolution reaction, ACS Nano 13 (2019) 5635–5645.